Full-Wave Pre-Stack Reverse-Time Migration by the Fourier Method and Comparisons with Kirchhoff Depth Migration

Ekkehart Tessmer

email: *ekkehart.tessmer@dkrz.de*
keywords: *Pre-Stack Reverse-Time Migration, Full-Wave, Pseudo-Spectral Method*

ABSTRACT

It is desirable to have a reference migration algorithm at hand when checking the quality of newly developed migration algorithms. Since full-wave reverse-time migration does not suffer from limitations due to high frequency approximation it is considered to fulfill this desire. Reverse-time migration is tested with different types of wave equations. Numerical examples show that the one-way wave equation works best, since only energy from direct wave paths are used for imaging. Tests with migration velocity errors up to 20% show that stable results (though mispositioned) are achievable. A comparison with reduced receiver density still yields useful results. Numerical tests show that strongly noisy data still allow reasonable imaging. Comparisons of reverse-time migration and Kirchhoff Migration results for the Picrocol model show that the reverse-time migration delivers a slightly better image.

INTRODUCTION

As a reference migration method a full-wave reverse-time pre-stack migration algorithm was implemented. This allowed to apply modifications to the algorithm, like using different types of wave equations. The algorithm is based on the Fourier method by Kosloff and Baysal (1982). It is also possible to implement the method using finite-differences. There are also different flavours regarding the implementation of the imaging condition like, e.g. Chang and McMechan (1986) who use ray tracing for the forward part of the migration or like, e.g. Schuster (2002) who uses for the forward and reverse parts full-wave modeling. The latter method appears more appealing, since it avoids limitation due to high frequency approximation methods.
In the first section the migration algorithm is explained and the basic equations are given. In the next section numerical tests of reverse-time migration for a simple subsurface model are performed and a comparisons with Kirchhoff depth migration are shown. In the third section comparisons of reverse-time and Kirchhoff depth migration for a larger data set (Picrocol) are presented.

THE PRE-STACK REVERSE-TIME MIGRATION ALGORITHM

Shot record pre-stack reverse-time migration algorithm is entirely based on numerical seismic modeling on a numerical grid. It is made up of two parts: (1) Forward modeling of acoustic waves for a shot through the macro-model with the source signature similar the one of the field recordings. (2) Reverse-time modeling of the shot record through the same subsurface macro-model. In both modelings for every subsurface point, i.e. gridpoint, time histories (seismograms) need to be recorded.

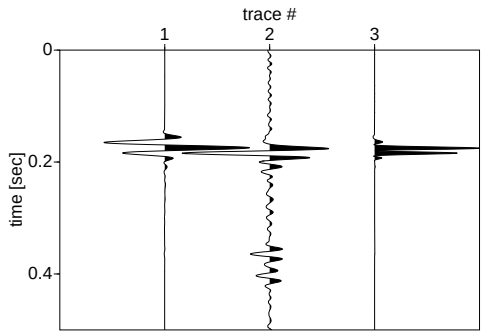

(a) Forward, reverse and product trace at (810 m, 440 m).

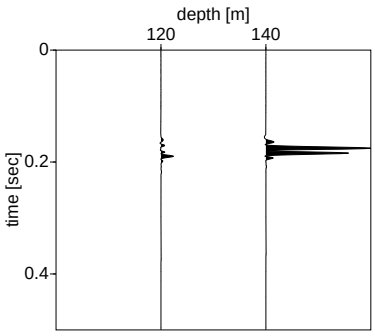

(b) Product traces off (120 m) and on (140 m) the reflector.

Figure 1: Sample subsurface traces for correlation.

In Fig. 1(a) Trace 1 and Trace 2 represent subsurface recordings from the forward and reverse part of the migration for the model shown in Fig. 2, respectively at the (x, z)-coordinates (810 m, 140 m). The image is then generated by zero-lag correlation, i.e. scalar product, of the two time traces for every subsurface grid point. The sample-wise product of the two traces before summing up is Trace 3 of Fig. 1(a). The idea is that energy is imaged at a reflector if from the shot down-going and from the geophones reverse downward propagated waves coincide. The product traces for a subsurface trace off and on a reflector are shown in Fig. 1(b). This imaging condition is based on the assumption that energy from the source to the point to be imaged belongs to the direct wave. On the other hand it assumes that reverse propagated energy belongs to single reflected waves, i.e. without multiples. If these conditions are not fulfilled energy will be imaged at places off reflectors. For reflectors without overhang this can be achieved, e.g. by using the one-way wave equation (Baysal et al., 1983). In case of an overhang one needs to allow two-way propagation and therefore is forced to suppress reflections. This can to a certain degree be achieved by applying impedance matching at the reflectors (Baysal et al., 1984) or by smoothing the background model (Kosloff et al., 1984). For the various tests the following 2-dimensional wave equations were used:

Two-way wave equation

$$\rho(x,z)\frac{\partial^2 p}{\partial t^2} = c^2(x,z)\left[\frac{\partial}{\partial x}\left(\frac{1}{\rho(x,z)}\,\frac{\partial p}{\partial x}\right) + \frac{\partial}{\partial z}\left(\frac{1}{\rho(x,z)}\,\frac{\partial p}{\partial z}\right)\right] \tag{1}$$

Constant-density two-way wave equation

$$\frac{\partial^2 p}{\partial t^2} = c^2(x,z)\left(\frac{\partial^2 p}{\partial x^2} + \frac{\partial^2 p}{\partial z^2}\right) \tag{2}$$

Impedance-matching two-way wave equation

$$\frac{\partial^2 p}{\partial t^2} = c(x,z)\left[\frac{\partial}{\partial x}\left(c(x,z)\,\frac{\partial p}{\partial x}\right) + \frac{\partial}{\partial z}\left(c(x,z)\,\frac{\partial p}{\partial z}\right)\right] \tag{3}$$

One-way wave equation

$$\frac{\partial p}{\partial t} = c(x,z)\; FFT_{xz}^{-1}\left[sign(k_z)\; i\; (k_x^2 + k_z^2)^{1/2} P\right] \tag{4}$$

where p is the pressure field, P is the pressure field double Fourier-transformed with respect to directions x and z, c is the velocity, ρ is the density, k_x and k_z are spatial wave numbers and FFT_{xz}^{-1} denotes a double inverse Fourier transform with respect to x and z. p, c and ρ are functions of the position.
Most of the computational work is needed for calculating the spatial derivatives. The spatial derivatives were computed by the Fourier method, which avoids numerical anisotropy and allows using coarse grid, i.e. two grid points per shortest wave length. Since computation of two first derivatives is about twice as costly as that of one second derivative it can easily be seen that Eqns. (2 and 4) can be solved about twice as fast as compared to Eqns. (1 and 3).
The time derivatives were replaced by the following finite-difference approximations:

$$\frac{\partial^2 p}{\partial t^2} \approx \frac{p(t+\Delta t) - 2p(t) + p(t-\Delta t)}{(\Delta t)^2}$$

and

$$\frac{\partial p}{\partial t} \approx \frac{p(t+\Delta t) - p(t-\Delta t)}{2\Delta t}$$

respectively. For extrapolation in time the resulting expressions are then solved for $p(t+\Delta t)$.

NUMERICAL TESTS WITH A SIMPLE VELOCITY MODEL

To examine the image quality based on the various types of wave equations for a simple model shown in Fig. 2 15 shot records were computed and subsequently the shots were muted, migrated and finally stacked (Figs. 4(a)-4(d)). The seismic velocities were 2000, 2500, and 3000 m/s and the densities were 1000, 1500, and 2000 kg/m^3, respectively. The model is gridded by spatial increments of 10 m, both, in horizontal and in vertical direction. The Ricker-like source wavelet had a dominant frequency of 50 Hz. Geophones were placed at any grid point at the surface, i.e. there were 143 traces at a spacing of 10 m recorded. For certain test cases the number of shots was increased or the number of geophones was decreased. This is explicitly stated in the respective description of the test.

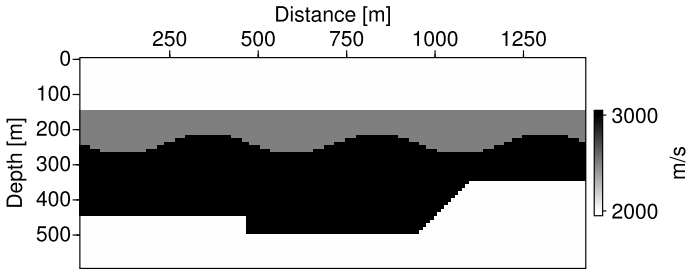

Figure 2: Velocity model.

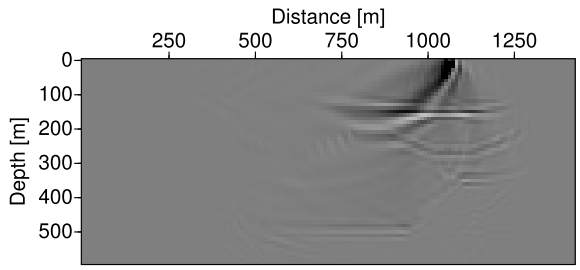

Figure 3: Migration of Shot 15.

Various wave equations

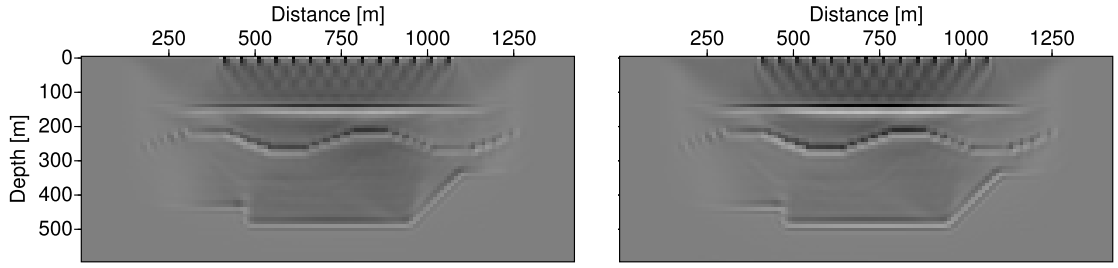

(a) Two-way WE.

(b) Two-way constant-density WE.

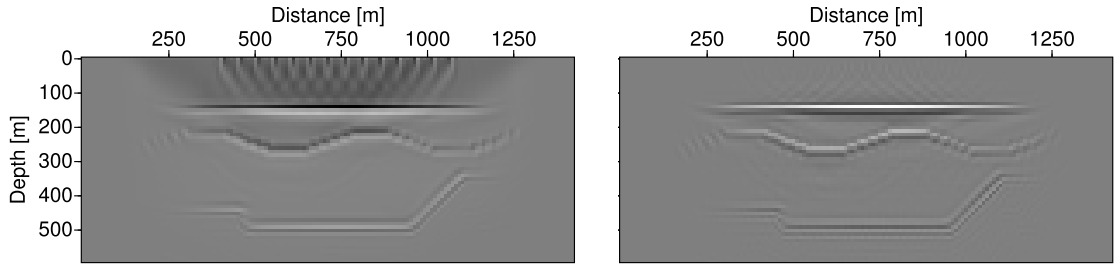

(c) Two-way non-reflecting WE.

(d) One-way WE.

Figure 4: Migration results for various types of wave equations.

At first glance the results look very similar. A closer look reveals that there are differences: in Figs. 4(a) and 4(b) some shades can be observed below the plane and the sinusoidal reflectors. This is due multiple reflections, which can develop in case of these two types of wave equations. In Figs. 4(c) and 4(d) these shades are not present.

Different number of shots

In Fig. 5 a comparison with different shot spacings is shown: 50 and 10 m, respectively. Apparently the amplitudes of the deeper reflectors were slightly enhances when using the higher number of shots. Both images are scaled according to their maximum.

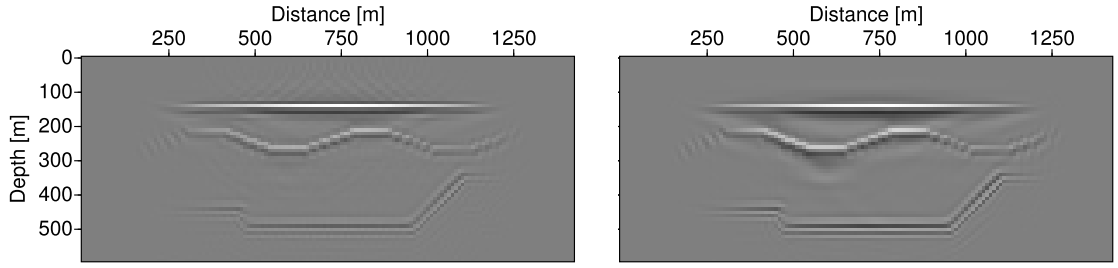

(a) One-way WE, 15 shots (same as 4(d)).

(b) One-way WE, 75 shots.

Figure 5: Comparison: 15 versus 75 shots with one-way wave equation.

Reduced number of traces

Figure 6 shows the migration result where only every 10th trace was used for input to the reverse modeling part of the migration procedure. 15 shots were stacked. The image quality degrades due to large geophone spacing (100 m).

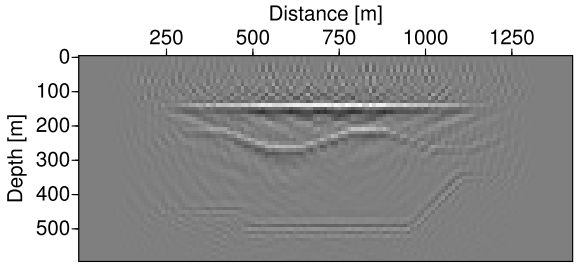

Figure 6: Migration with only every 10th trace.

Noisy data

Figure 7 shows that migrating data with signal/noise ratio of one (15 shots) gives reasonable results, whereas an S/N ratio of 0.2 obscures the deeper horizons.

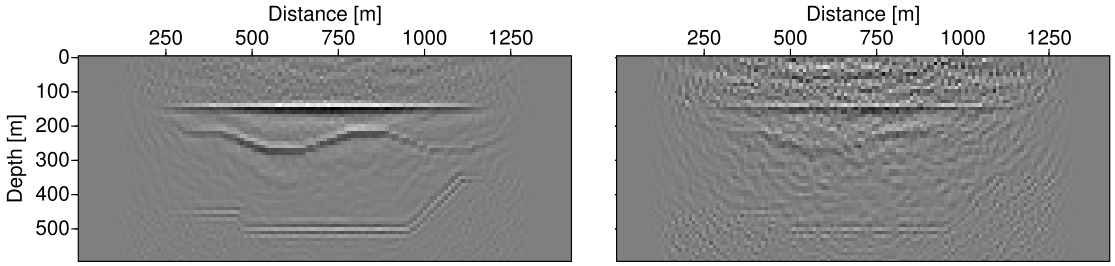

(a) S/N ratio = 1.

(b) S/N ratio = 0.2.

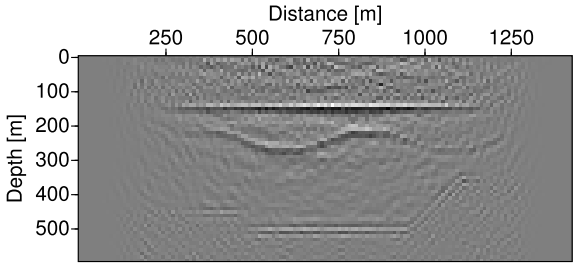

(c) S/N ratio = 0.2 with a 5 times higher shot density compared to Fig. 7(b).

Figure 7: Migration of data with different S/N ratios.

The comparison of Figures 7(b) and 7(c) demonstrates the well known fact that increasing the number of shots (stacking fold) can cure the problem of noise.

Migration velocity errors

Figures 8 and 9 show results with 10 and 20 percent too low and too high migration velocities. The same relative velocity error was applied to the entire velocity field.

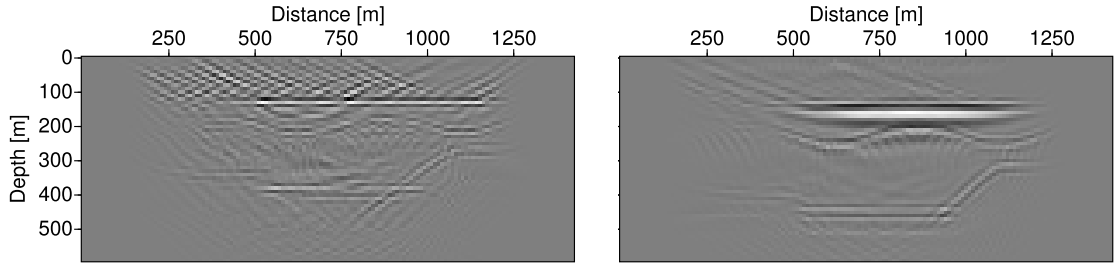

(a) $Vp/Vp_0 = 0.8$ **(b)** $Vp/Vp_0 = 0.9$

Figure 8: Too low migration velocities.

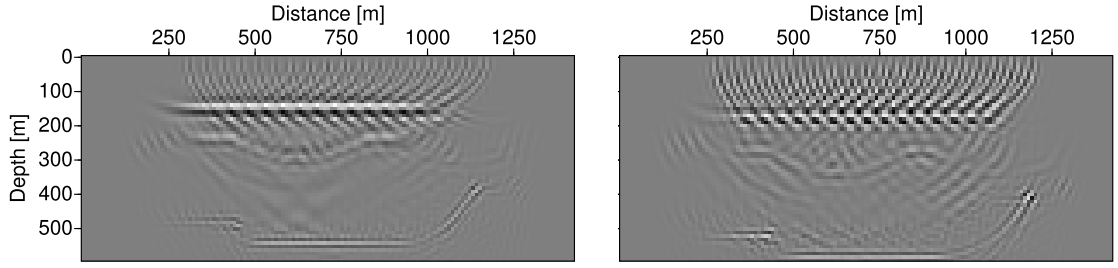

(a) $Vp/Vp_0 = 1.1$ **(b)** $Vp/Vp_0 = 1.2$

Figure 9: Too high migration velocities.

Smoothing the macro model

To show the influence of smoothing (i.e. some sort of averaging) of the velocity model migrations with different degrees of slowness smoothing were performed. The smoothing procedure was applied to inverse velocities, i.e. slownesses. Slowness smoothing was chosen because it had turned out that it is better able to approximately preserve the total traveltimes than averaging directly the seismic velocities. The smoothing operator has the weights $\frac{1}{4}, \frac{1}{2}, \frac{1}{4}$ in each direction. The results are shown in Fig. 10. Even in case of very strong smoothing the shape of the reflectors are well reconstructed. However, they are mispositioned (see e.g. the deepest reflector).

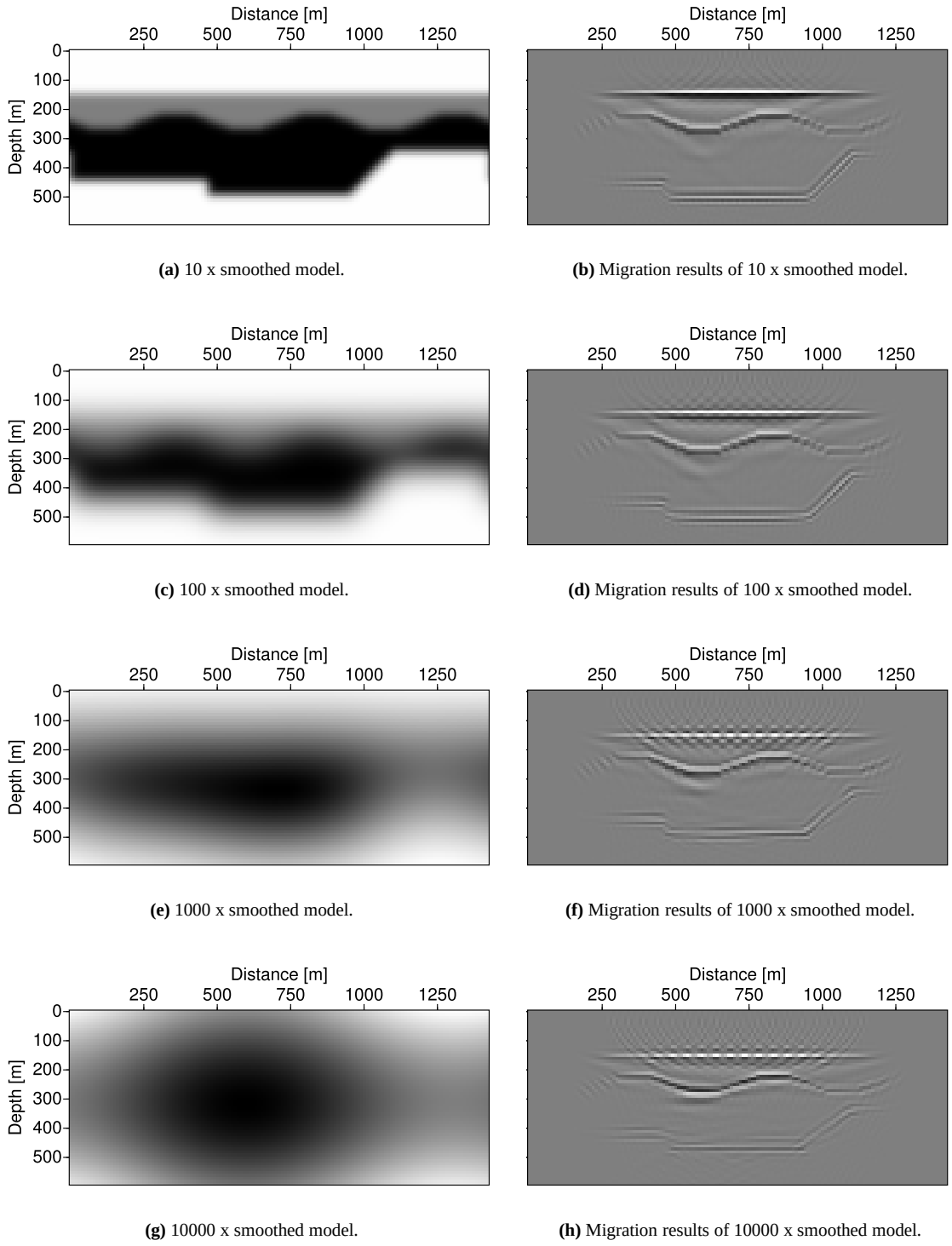

(a) 10 x smoothed model.

(b) Migration results of 10 x smoothed model.

(c) 100 x smoothed model.

(d) Migration results of 100 x smoothed model.

(e) 1000 x smoothed model.

(f) Migration results of 1000 x smoothed model.

(g) 10000 x smoothed model.

(h) Migration results of 10000 x smoothed model.

Figure 10: Migration results from different degrees of slowness smoothing.

Kirchhoff migration for comparison

A comparison of the reverse-time and Kirchhoff pre-stack depth migration results are given below. The traveltime tables were generated with the wave front oriented ray tracing (WRT) by Coman and Gajewski

(2001). Trying to use SU's RAYT2D it delivered incomplete traveltime tables, i.e. at many grid points no traveltimes were computed. Therefore the latter algorithm could not be used. Compared to the reverse-time migration results it becomes obvious, that the amplitudes (reflectivities) of the reflectors are different. Apparently the lower reflectors are of lower amplitude in the reverse-time migration compared to the Kirchhoff results. This can be explained by the fact, that the amplitude of the direct wave in the forward part of the migration procedure suffers from geometrical spreading. The result is that the correlation of the traces from the forward and the reverse modeling is weaker at greater depth.

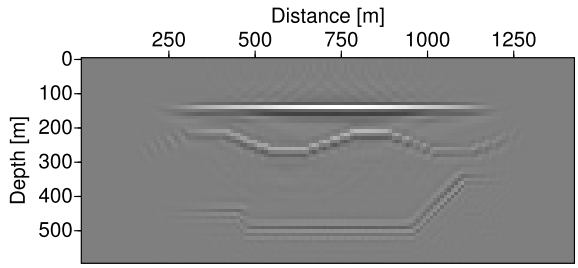

(a) Figure 4(d) (repeated).

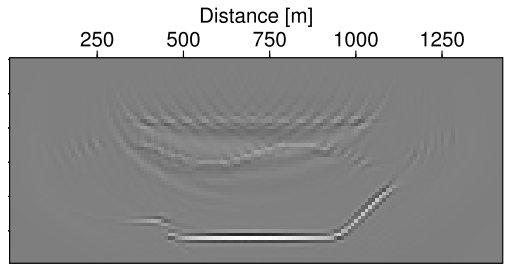

(b) Kirchhoff migration result, 100 x smoothed.

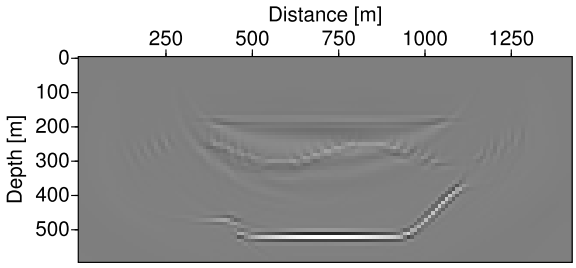

(c) Like Fig. 11(b) but 75 shots.

Figure 11: Comparison of reverse-time and Kirchhoff migration results.

The Kirchhoff migration result in Fig. 11(b) obviously suffers much more from the low shot density than reverse-time algorithm. Increasing the number of shots by a factor of five (Fig. 11(c)) lets the top reflector appear continuous.

Geometrical spreading compensation

For compensating the geometrical spreading of the forward modeling part the recorded subsurface traces were normalized by its individual RMS, maximum, or L1-norm value of amplitude. The results without and with normalization are shown in Fig. 12. It is assumed that for the reverse modeling part no compensation for geometrical spreading is necessary, since the wave field excited from the receivers reverse in time will be focussed at the reflectors.

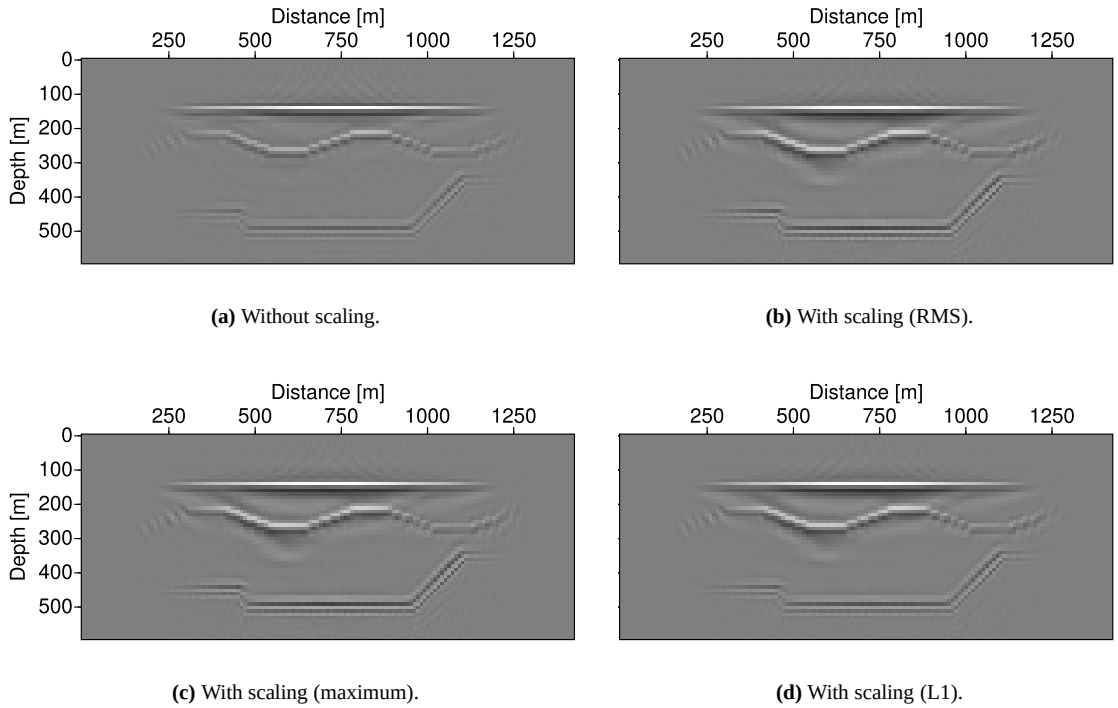

(a) Without scaling.

(b) With scaling (RMS).

(c) With scaling (maximum).

(d) With scaling (L1).

Figure 12: Comparison of migration results without and with normalization.

MIGRATING THE PICROCOL MODEL

The synthetic data for the Picrocol model were computed by the Fourier method. The size of the model was 14 km in horizontal and 4.12 km in vertical direction with a spatial discretization of 5 m. The velocities varied between 1700 and 5000 m/s. The velocity model is shown in Fig. 13.
81 shot records were generated where the total propagation time was 3 seconds. The shot distance was 100 m. An end-on configuration was used, where the shot location was to the left of the receivers. The first and last shot was located at 1 km and 9 km, respectively. The number of receivers was 207 with a spacing of 20 m. The offsets were between 0-4120 m.
The data were muted to remove the direct wave. In addition they were high-pass filtered to get rid of artifacts from boundary reflections.

Reverse-time migration of the Picrocol data set

The migration algorithm is based on a grid with a dicretization of 10 m, which fulfills the spatial Nyquist condition. The timestep size was 0.4 ms, in total 7500 steps.

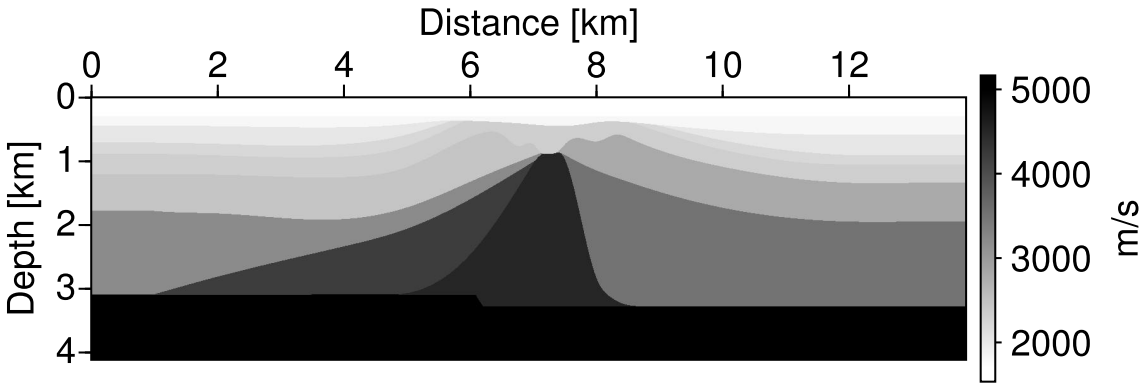

Figure 13: The Picrocol velocity model.

Comparison of migration results from the reverse-time migration using offsets up to 1000 m and all available offsets, respectively, are shown in Fig. 14.

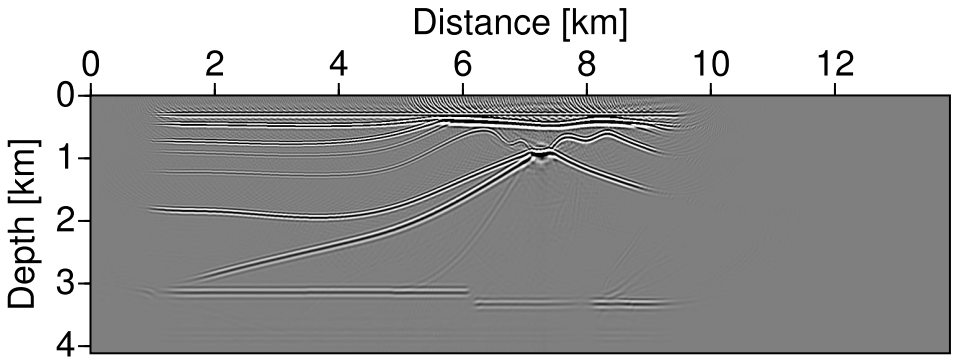

(a) Offsets up to 1000 m.

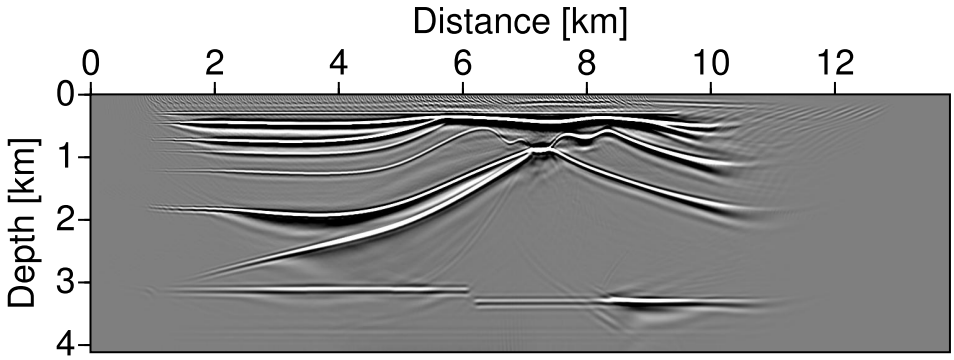

(b) All available offsets.

Figure 14: Reverse-time migration results of the Picrocol model with different offset ranges.

The image based on a limited number of offset appears more clear than the image with all available offsets. It is not completely clear, why the reflectors appear less sharp in the latter case. A possible explanation is that the synthetic data contain artifacts, like boundary reflections.

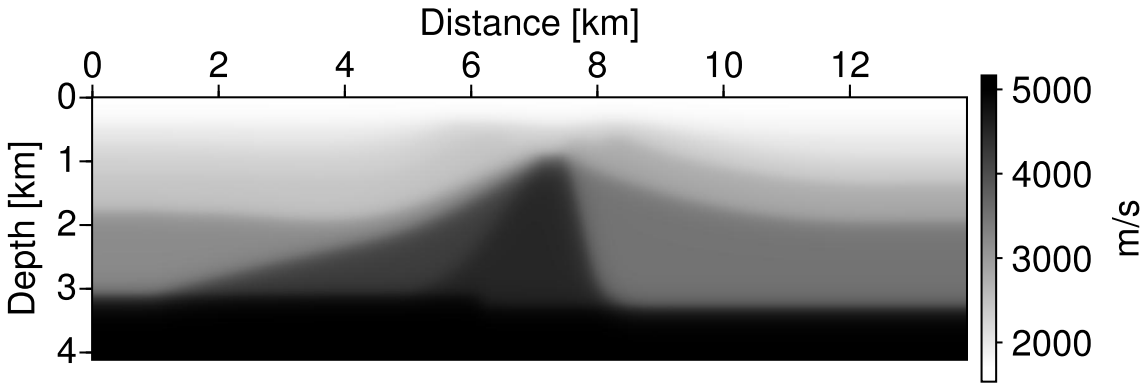

Figure 15: The smoothed Picrocol model.

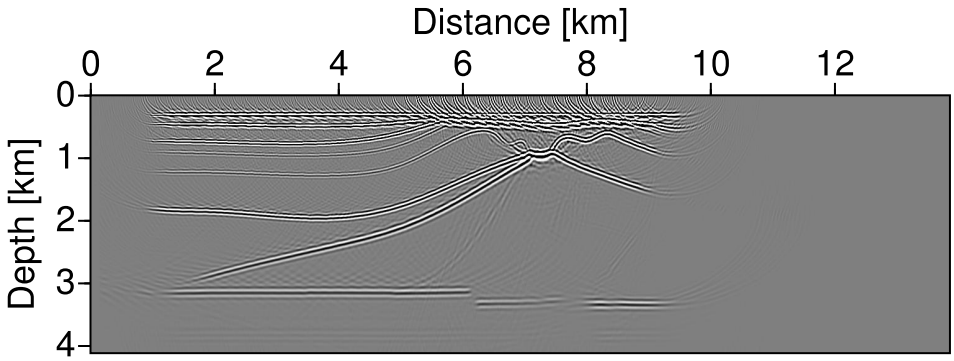

(a) Offsets up to 1000 m.

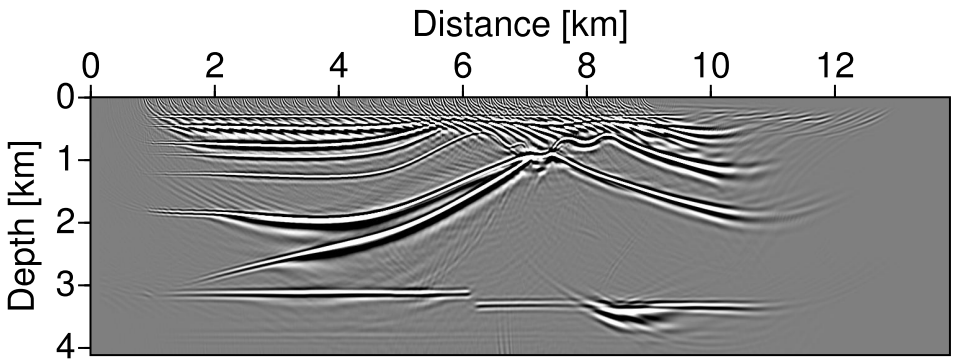

(b) All available offsets.

Figure 16: Reverse-time migration results with smoothed Picrocol model with different offset ranges.

Also the results based on a smoothed macro model suffer from artifacts when using the whole offset range for the shot gather migration.

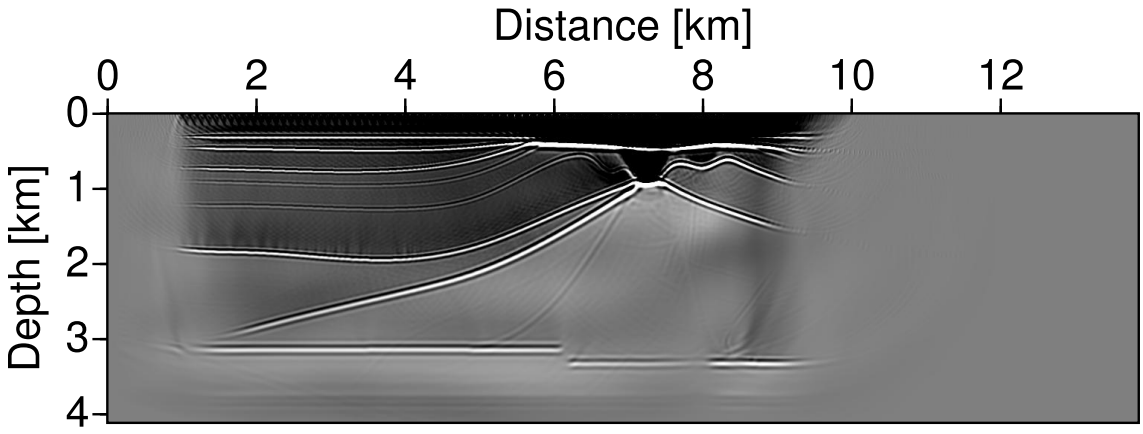

Figure 17: Migration results of the Picrocol model applying the constant-density wave equation.

To show the effect of energy being reflected between interfaces the same data set was migrated using the constant-density wave equation, which allows propagation of multiple reflections. Here offsets up to 1000 m were used. As can be seen in Fig. 17, due to imaging of multiples at wrong locations as described earlier, strong shading between the interfaces appears, especially at the upper portion of the model.

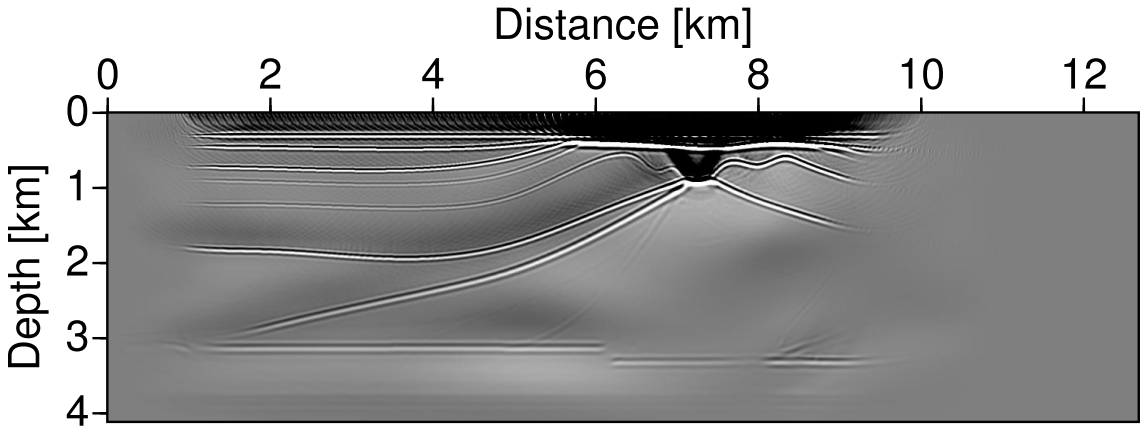

Figure 18: Migration results of the Picrocol model applying the impedance-matching wave equation.

Figure 18 shows migration results using the impedance-matching two-way wave equation with offsets up to 1000 m. Comparing the results to Figs. 14(a) and 17 it can be seen that the impedance-matching wave equation produces more artifacts than the one-way wave equation but less than the constant-density wave equation.

Kirchhoff depth migration of the Picrocol data set

For comparison with the reverse-time migration results from the Kirchhoff depth migration using offsets up to 1000 m and all available offsets, respectively, are shown in Fig. 19. Because of the algorithm (wave front oriented ray tracing) for traveltime table generation the migration is based on a smoothed version of the Picrocol velocity model.

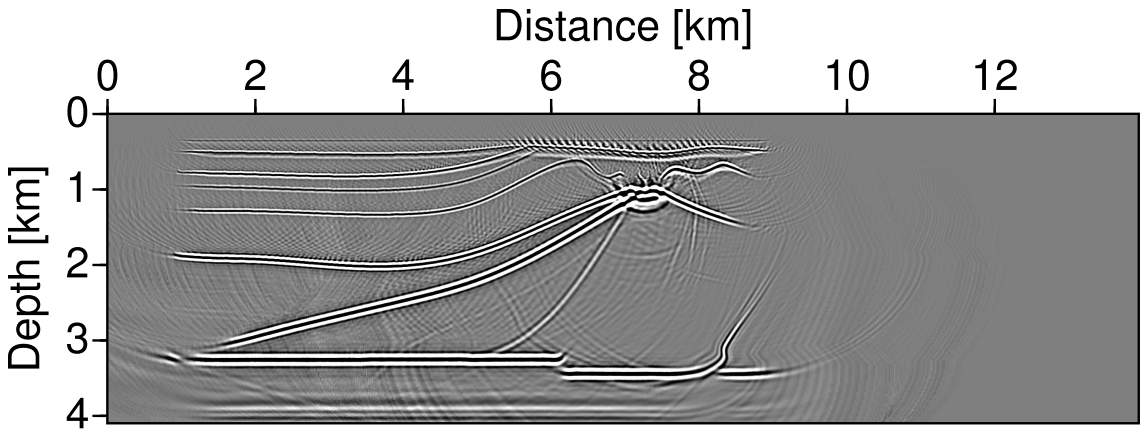

(a) Offsets up to 1000 m.

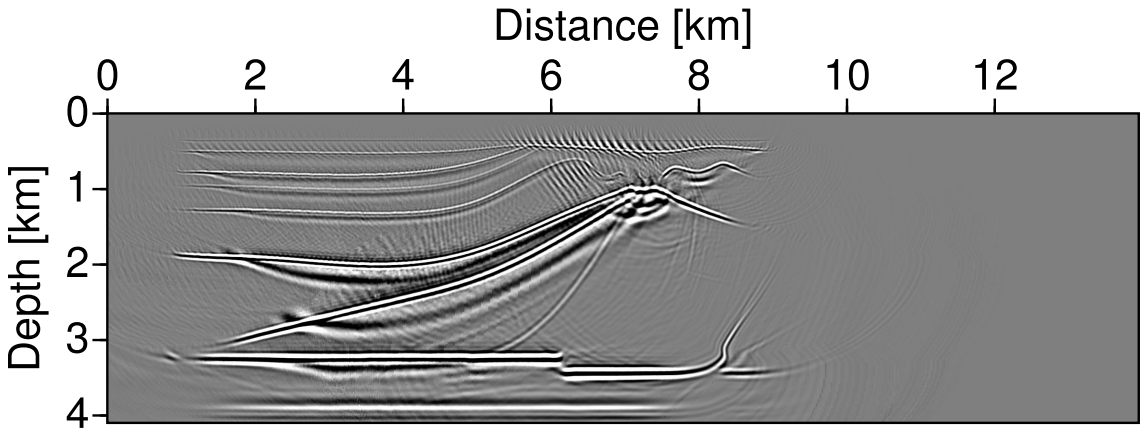

(b) All available offsets.

Figure 19: Kirchhoff migration results of the Picrocol model with different offset ranges.

Comparing the reverse-time and Kirchhoff migration results there are no striking differences. However, the horizons in the image of the reverse-time migration has a larger extension to the right. The reason for this is not clear, since in both methods the same number of shots with the same offsets were migrated. In the case of migration with all offsets also the Kirchhoff migration shows some artifacts below the reflectors. Like in the simple test case the deeper reflectors are stronger here similar to the case of the reverse-time migration.

CONCLUSIONS

Tests with synthetic data under controlled conditions showed that reverse-time pre-stack depth migration produces good results, which partly are superior to the ones obtained by Kirchhoff depth migration. The test show in particular that the method is quite stable with respect to errors in migration velocities, macro model smoothing, noise contamination of the shot records, and to shot and receiver density. Reverse-time migration has no restrictions regarding the smoothness of the macro model, like certain algorithms for traveltime table calculation. One needs to decide carefully, which wave equation is to be used in order to resolve certain structural features, like overhangs. In the present form the reverse-time migration does not produce 'true amplitudes'. The CPU time requirements are very high compared to Kirchhoff migration:

For the case of the Picrocol model a factor of about 60 more CPU time was used. For the future it is planned to search for ways to improve the efficiency of the above described reverse-time pre-stack depth migration.

ACKNOWLEDGMENTS

Colorado School Of Mines' Seismic Unix (SU) was used for certain processing steps and for the generation of figures. This work was supported by the University of Hamburg.

REFERENCES

Baysal, E., Kosloff, D., and Sherwood, J. (1983). Reverse-time migration. *Geophysics*, 48:1514–1524.

Baysal, E., Kosloff, D., and Sherwood, J. (1984). A two-way non-reflecting wave equation. *Geophysics*, 49:132–141.

Chang, W. F. and McMechan, G. A. (1986). Reverse-time migration of offset vertical seismic profiling data using the exitation-time imaging condition. In *Geophysics*, volume 51, pages 67–84. Soc. of Expl. Geophys.

Coman, R. and Gajewski, D. (2001). Estimation of multivalued arrivals ind 3-D models using wavefront ray tracing. In *Expanded Abstracts*, pages 1265–1268.

Kosloff, D. and Baysal, E. (1982). Forward modeling by a Fourier method. *Geophysics*, 47:1402–1412.

Kosloff, D., Reshef, M., and Loewental, D. (1984). Elastic forward modeling by the Fourier method. *Geophysics*, 49:634–634.

Schuster, G. (2002). Reverse-time migration = generalized diffraction stack migration. In *72nd Ann. Internat. Mtg*, pages 1280–1283. Soc. of Expl. Geophys.